JOURNAL OF AIRCRAFT
Vol. 44, No. 4, July–August 2007

Aerodynamic Loading for an Airfoil with an Oscillating Gurney Flap

Deman Tang* and Earl H. Dowell†
Duke University, Durham, North Carolina 27708-0300

DOI: 10.2514/1.26440

A study of aerodynamic loadings on a NACA 0012 airfoil with a static and an oscillating trailing-edge Gurney flap was made. The focus is on the experimental measurement of the static and dynamic-pressure distributions on the airfoil surface. The experimental results are also correlated with theoretical results obtained using the Navier–Stokes code INS2D, developed by NASA. A Reynolds number of 348,000, a flow velocity of 20 m/s (65.6 ft/s), and a reduced frequency from 0 to 0.4 based upon half-chord b and freestream velocity U are used. The experimental results show that the effect of the static and oscillating strips located near the trailing edge of the airfoil is to enhance the maximum lift and pitching-moment coefficients for both unstalled and stalled angles of attack. An increase of the oscillating frequency also enhances the aerodynamic loading. Reasonably good agreement between the experiment and theory is obtained. The experimental results confirm the idea that an oscillating small strip located near the trailing edge can be a useful tool for active aerodynamic flow control for a wing.

Nomenclature

b	=	half of an airfoil chord
C_l	=	lift coefficient
C_m	=	pitching-moment coefficient
C_p	=	pressure coefficient
$\bar{C}_p$	=	averaged pressure coefficient
c	=	airfoil chord
H^{cl}, H^{cm}	=	lift and pitching-moment transfer functions
h	=	oscillating amplitude of a Gurney flap
h_s	=	static Gurney flap height
k	=	reduced frequency
Re	=	Reynolds number
t	=	physical time
U	=	flow velocity
α	=	angle of attack
Ψ^{cl}, Ψ^{cm}	=	lift and pitching-moment phase-shift angles
ω, f	=	oscillating frequency, $\omega = 2\pi f$

Introduction

THE aerodynamic effect of a small strip mounted on the pressure-side trailing edge of an airfoil has been studied for several decades. Work by Liebeck [1] showed that a small Gurney flap (GF) increases the maximum lift coefficient and decreases the angle of attack of zero lift, whereas the lift curve slope remains relatively constant. Jeffrey et al. [2] and Van Dam et al. [3] studied the experimental aerodynamics of Gurney flaps on a single-element high-lift wing and on an airfoil. These experimental data indicate that there is a von Kármán vortex sheet of alternately shed vortices present in the wake downstream of a Gurney flap that increases the aerodynamic loading on both the suction and pressure sides of the airfoil. These changes result in a larger pressure difference acting across the trailing edge and generate an increase in circulation. Storms and Jang [4] provided static experimental results for the lift enhancement of an airfoil using a Gurney flap and vortex generators. The addition of a Gurney flap increased the maximum lift coefficient from 1.49 to 1.96 and decreased the drag near the maximum lift condition for a NACA 4412 airfoil. The application of vortex generators to the baseline airfoil yielded an increase in the maximum lift coefficient of 0.34. with respect to the no-GF configuration.

The published experimental and computational results are mostly for the static Gurney flap case. For an oscillating small strip or an oscillating airfoil with a fixed small strip near the trailing edge of the airfoil, previous theoretical and experimental work is sparse up to now. Greenblatt et al. [5,6] observed that both light and deep stall can be controlled using periodic excitation. They also observed that the periodic excitation was superior to steady blowing. All of the previous experimental and computational studies have been with the airfoil oscillating in an oncoming steady flow. However, it is also of interest to study the fluid physics of an oscillating airfoil fitted with a fixed Gurney flap as well as a fixed airfoil fitted with an oscillating Gurney flap beyond the static stall angle of attack. Work by Tang et al. [7] focused on computational prediction for both the oscillating airfoil and the oscillating Gurney flap. An incompressible Navier–Stokes code, INS2D, developed at NASA Ames Research Center, was employed for this purpose. The theoretical results were correlated with the dynamic experimental results for an oscillating wing with small fixed trailing-edge strips provided by Gerontakos and Lee [8]. It is also interesting to investigate the effect of Gurney flaps on the hysteresis observed in the aerodynamic-load loops of an oscillating airfoil for a given Gurney flap height from 1.6 to 3.2% chord.

The present work focuses on the experimental measurement of the static and dynamic-pressure distribution on the airfoil surface when the small strip oscillates. The results are also computationally examined using a Navier–Stokes code, INS2D, as described in [7]. The present results may be helpful in better understanding the mechanism of lift enhancement and possible strategies for aerodynamic flow control. Note that the investigation here is concerned with using an oscillating Gurney flap as a possible dynamic flow control device over a range of dynamic frequencies. For static flow characteristics per se, an oscillating Gurney flap may have no particular advantage. Possible dynamic flow control applications might include rotorcraft and aeroelastic dynamic flows or unsteady aerodynamics as well as aeroacoustics (though the latter would require much higher reduced frequencies than those considered here). In a very recent study of wake vortex control using *static* segmented Gurney flaps, Matalanis and Eaton [9] suggested that "miniature trailing edge effector configurations, if varied in time, may be useful for wake alleviation."

Received 10 July 2006; revision received 21 March 2007; accepted for publication 22 March 2007.

*Research Associate Professor, Department of Mechanical Engineering and Materials Science.

†William Holland Hall Professor, Department of Mechanical Engineering and Materials Science and Member of the Center for Nonlinear and Complex Systems.

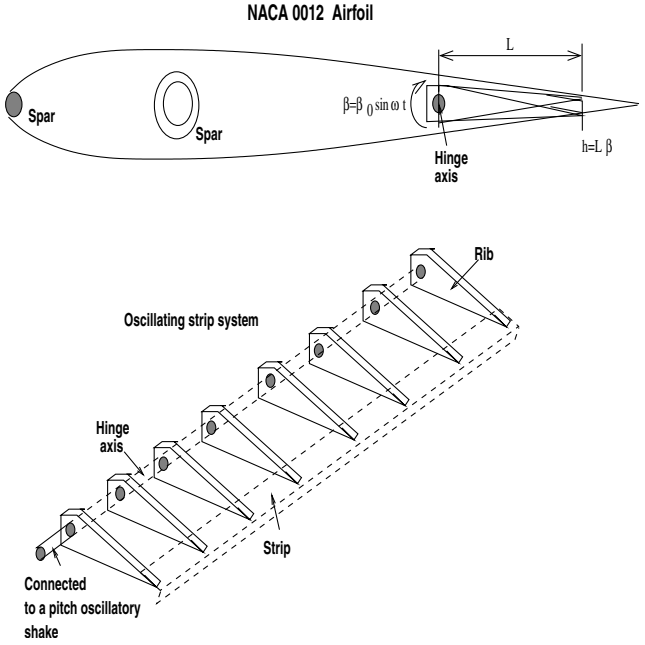

Fig. 1 Schematic of the oscillating strip.

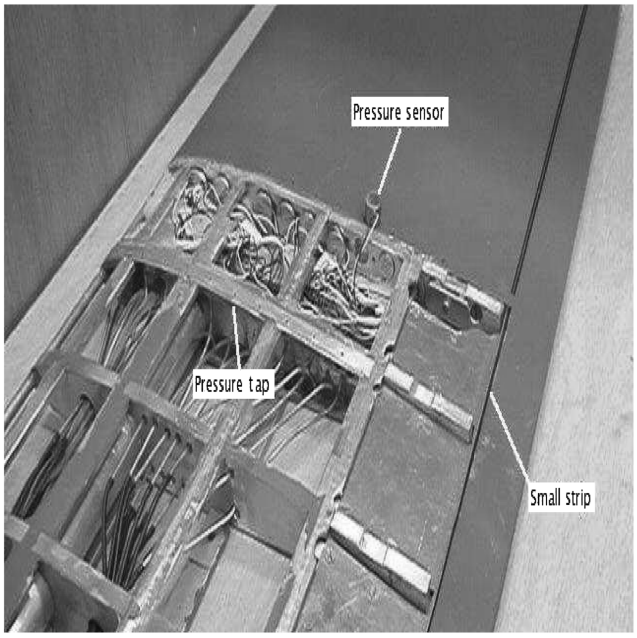

Fig. 3 Photograph of the airfoil model and the pressure measurement system.

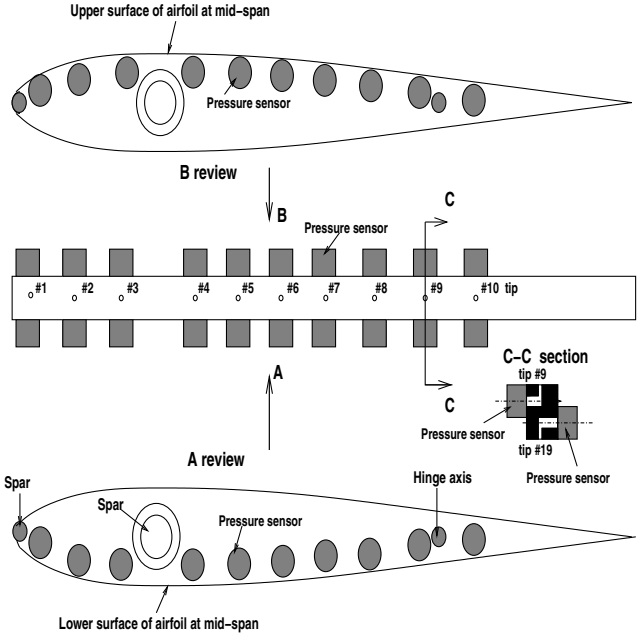

Fig. 2 Schematic of the pressure measurement system.

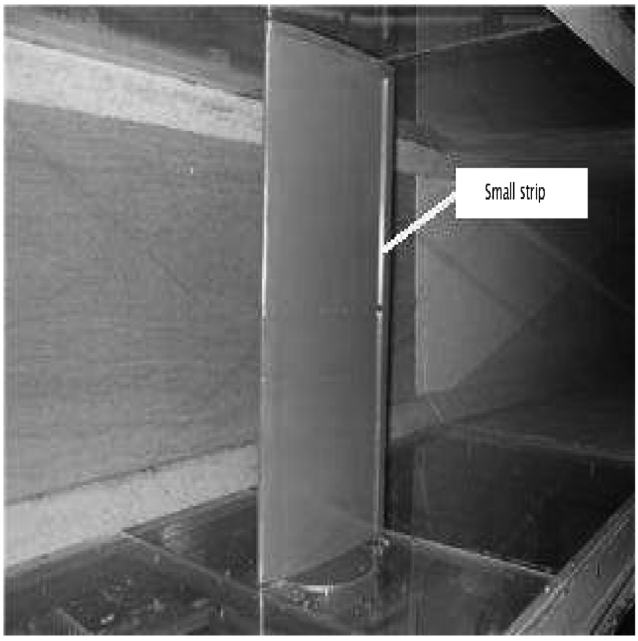

Fig. 4 Photograph of the airfoil model in the wind tunnel.

Description of Experiment

Experimental Model

All steady- and unsteady-state response tests of the two-dimensional wing model with an oscillating small strip were performed in the Duke University low-speed wind tunnel. The wind tunnel is a closed-circuit tunnel with a test section of 0.7×0.53 m^2 (2.3×1.75 ft^2) and a length of 1.52 m (5 ft). The maximum air speed attainable is 89.3 m/s (293 ft/s). The stagnation temperature of the airstream is held constant over the range 60 to 100°F by means of an external air exchange system, and tunnel stagnation pressure equals atmospheric pressure at the low Reynolds number operating conditions. For the present test, the Reynolds number was 0.348×10^6 and the reduced frequency of the strip oscillation, $\omega b/U$, was varied up to a value of 0.4.

To observe the dynamic-pressure distribution and measure the aerodynamic loading due to a small oscillating strip mounted near the trailing edge through wind-tunnel tests, a typical wing section model was constructed. Design of the typical section took into account the fact that it must accommodate an oscillating strip near the trailing edge and 20 micropressure sensors (PCB model 103B01) at the midspan and also be mounted in the Duke University wind tunnel using an existing pitch-oscillating testing rig. This position of the Gurney flap was selected as one of the two obvious choices, the other being near the leading edge of the airfoil. Either position could have been used. The trailing edge was chosen simply because this seems to be a position more commonly used in practice.

The profile of the typical section is a NACA 0012 symmetrical airfoil, having a chord length of 0.2554 m (10 in.), which nicely accommodates an oscillating strip located at 90% chord, and 20

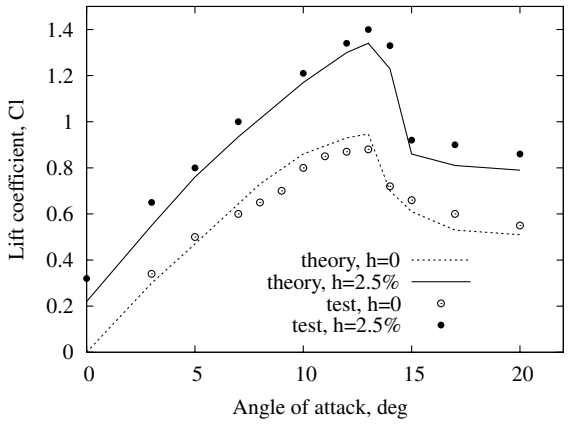

a)

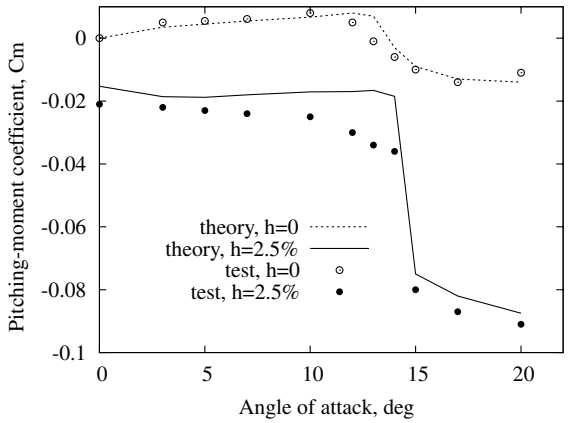

b)

Fig. 5 Comparison between calculation and experiment for the a) lift and b) pitching-moment coefficients vs angle of attack at $Re = 348,000$.

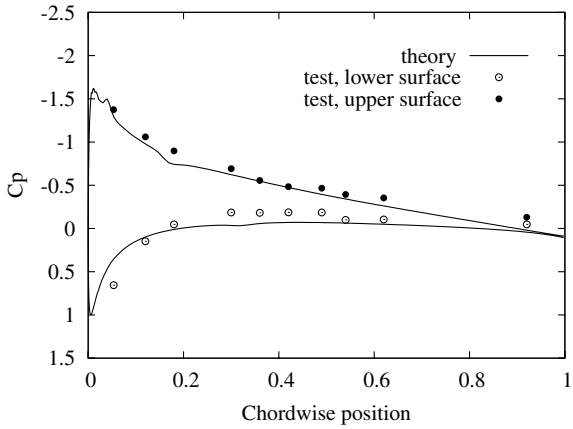

a)

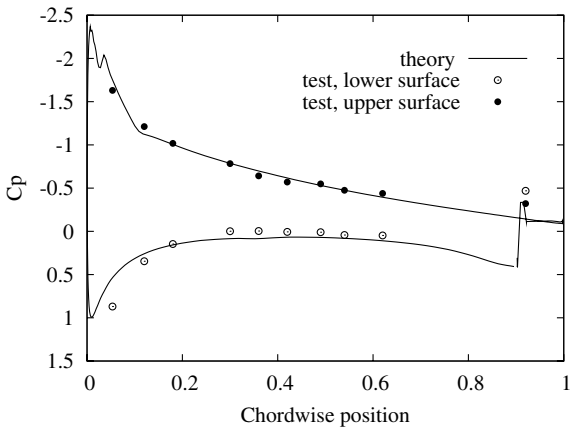

b)

Fig. 6 Static-pressure distribution at $Re = 348,000$ and $\alpha = 5$ deg for a) $h = 0$ and b) $h = 2.5\%$.

pressure sensors. The span $l = 0.52$ m (1.7 ft) of the typical section was dictated by the height of the wind tunnel, because the typical section is to be mounted vertically. Eight pieces of NACA 0012 airfoil ribs made of aluminum material with 0.64-cm (0.25-in.) thickness are used for high chordwise stiffness and for adequate housing for bearings supporting the small-strip hinge. In addition, a midspan aluminum rib with 1.27-cm (0.5-in.) thickness provides support for 20 pressure sensors. The airfoil ribs are placed on three spars that, in addition to being structural elements, have specific functional roles. The spar placed at the quarter-chord is an aluminum tube and serves to mount the model on the testing rig that is connected to a very heavy support frame that is attached to the ground. The spar placed at the leading edge provides support for the skin and additional reinforcement of the leading edge. The spar placed at 69% chord is a hinge axis of the oscillating strip that is mounted on nine airfoil ribs through bearings supporting the strip.

As shown in Fig. 1, the Gurney flap is made of a aluminum sheet 0.508×0.0254 m (20×10 in.) with 0.51-mm (0.02-in.) thickness and a bent 90-deg angle at one-fourth width of the sheet, that is, the small-strip height is 2.5% chord. The strip is fixed to the end of the eight special rib elements. The rib elements are bolted to the hinge axis. Thus, when the hinge axis is torsionally oscillated, a small-strip oscillation is obtained, as shown at the top of Fig. 1.

The midspan airfoil rib is specially made to measure the dynamic-pressure distribution at midspan and provide support for the 20 micropressure sensors. There are 20 orifices of 1.16-mm (0.046-in.) diameter for the pressure taps, which are symmetrically distributed over the upper and lower surfaces, respectively. The orifice positions in terms of percentage chord from the leading edge are 0.06, 0.12, 0.18, 0.3, 0.42, 0.49, 0.54, 0.61, and 0.74. The pressure sensor is bolted on the midspan airfoil rib and installed with an adhesive mounting ring to prevent a pressure leak between the pressure surface of the sensor and the airfoil orifice. [The dimensions of the pressure sensor are 9.5-mm (0.374-in.) diameter and 7-mm (0.27-in.) height. The weight is 3.26 g. The signal/noise is 60 dB, that is, the uncertainty is 0.1%. The dynamic range is 77 dB and the frequency range is 5 to 13 kHz]. Details of the dynamic-pressure measurement device are shown in Fig. 2.

All of the structural elements are held together by epoxy resin and mechanical elements (bolts, pins, etc.). They are covered with 0.25-mm-thick (0.01-in.) aluminum foil (called skin).

Static and dynamic-pressure measurements are made with separate sets of transducers due to the inability of the latter to sustain large static pressures. To measure the static or steady-state pressure distribution, a separate set of 20 orifices of 1.16-mm (0.045-in.) diameter for the pressure taps are also symmetrically distributed over the upper and lower surfaces on an airfoil rib that is located at a 0.45 span from the root. The orifice position along the chord is the same as for the orifices for the dynamic-pressure transducers at the midspan airfoil rib, except for the last orifice, which is at 0.74 of the chord. The last dynamic orifice (upper and lower surface) is located at 0.92 of the chord that is near the small Gurney flap (0.9 of the chord). Twenty plastic tubes with 1.16-mm (0.045-in.) i.d. and connecting elements are permanently bonded on the 20 orifices of the airfoil rib by epoxy. After installing each set of orifice and tube, they were all sealed and the sealant was sanded smooth to conform to the local airfoil contour. The 20 tubes were connected to the input end of a 20/10 channel air switch. This switch has two switching positions corresponding to the upper and lower surface taps of the airfoil model. Experience indicates that the air leakage in the switch may be a very important

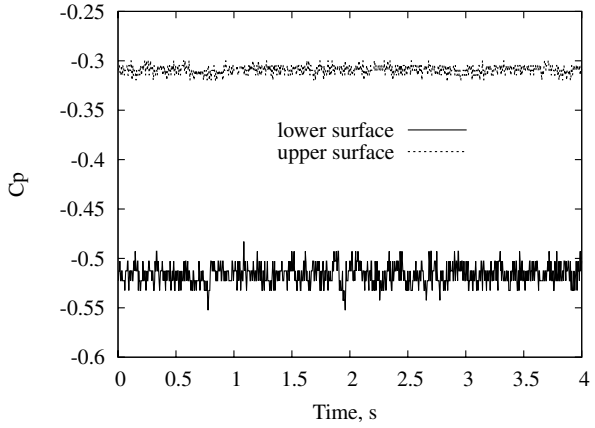

a)

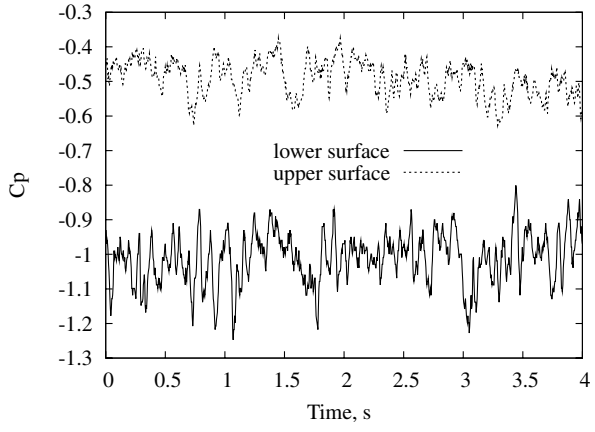

b)

Fig. 7 Time history of pressure coefficient at $x/c = 0.92$ and $Re = 348,000$ for 2.5%c for a) $\alpha = 5$ deg and b) $\alpha = 15$ deg.

problem. As shown in a leakage test, the air leakage is irregular and leads to pressure interaction between adjacent channels. After some development, a more completely sealed and reliable air switch configuration that overcame this problem was used in this test.

The output end of the switch is connected to 10 pressure transducers (Omega PX163). The transducer measures pressure in the very low range, ±0.127-m (5-in.) H_2O, and features excellent sensitivity with a nominal value of 13.84 V/psi at 9-V excitation, which is much higher than the sensitivity of the miniature pressure transducer (10 mV/psi). Before testing, all pressure transducers were individually calibrated. The wind tunnel provided an exact pressure head from 0.01-m (0.4-in.) H_2O to 0.051-m (0.2-in.) H_2O relative to local atmospheric pressure. The output data of each transducer subjected to these pressures were recorded. The calibration curves are essentially linear.

The Gurney flap excitation was performed by a pitch oscillatory shake table that is mounted to a very heavy support frame that is attached to the ground. The shake table is driven using a dc servomotor through a cam. The driving frequency is controlled by a D/A NB-MIO-16 system. A nearly pure single harmonic excitation is provided. A photograph of the wind-tunnel model and the pressure measurement system in the model is shown in Fig. 3.

Measurement Data Acquisition

For the dynamic-pressure measurement, the output of each pressure sensor and strip oscillating displacement was directly recorded on a PC computer through signal conditioners (PCB models 481A02 and 442C04) and a data acquisition package (NB-MIO-16), which consisted of a 16-channel A/D plug-in interface board, a BNC termination box, and data acquisition and analysis software,

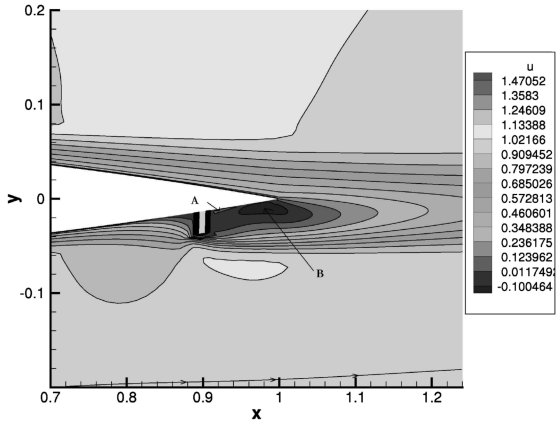

Fig. 8 Velocity u contours for the 2.5%c at $Re = 348,000$ for $\alpha = 5$ deg; note the y scale was exaggerated for clarity.

LabView version 7.0. Other four-channel pressure signals and the strip oscillating signal are recorded in the multi-analyzer system, PULSE 3560. The sampling rate was not less than 50 points per oscillatory cycle. The total number of data points vary with the strip oscillating frequency.

Because of unavoidable freestream and boundary-layer turbulence irregularities, each cycle of pressure measurements was found to be slightly different in the range below the stall angle of attack and distinctly different in the stalled portion of the cycle. The freestream turbulence levels are about 1% of the nominal velocity. To remove this randomness from the pressure data, an ensemble-averaging procedure over a number of cycles was carried out. The lift-force and

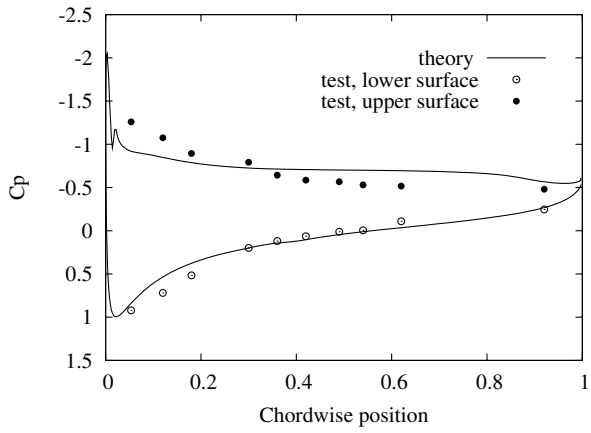

a)

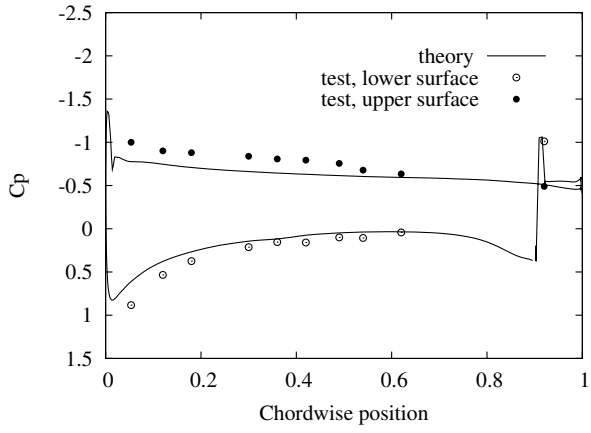

b)

Fig. 9 Static-pressure distribution at $Re = 348,000$ and $\alpha = 15$ deg for a) $h = 0$ and b) $h = 2.5\%$.

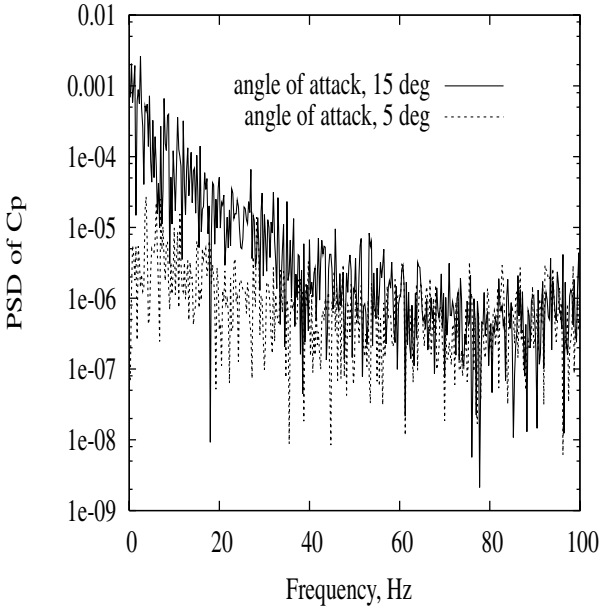

Fig. 10 PSD of the pressure coefficient at $x/c = 0.92$ and 2.5%c.

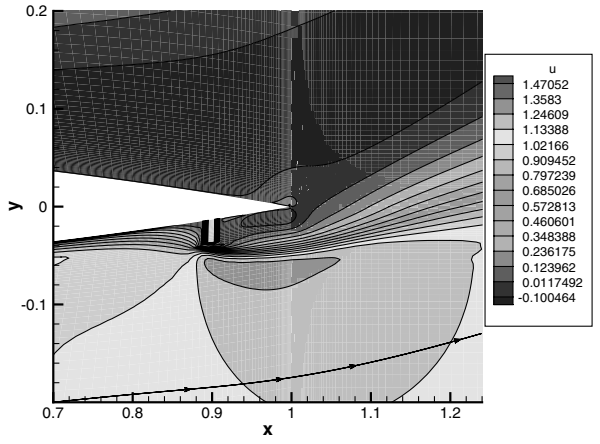

Fig. 11 Velocity contours for 2.5%c at $Re = 348,000$ for $\alpha = 15$ deg; note the y scale was exaggerated for clarity.

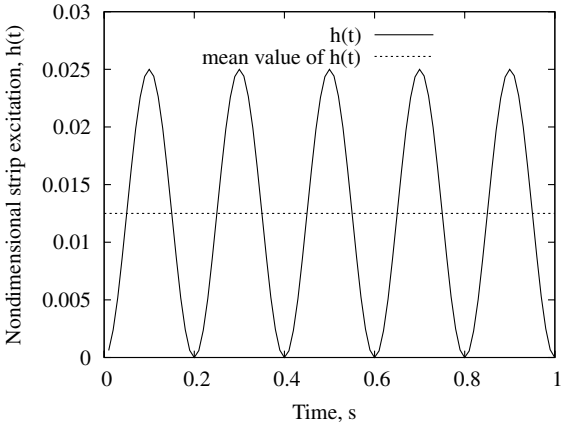

Fig. 12 Time history of the small-strip excitation at frequency $\omega = 5$ Hz.

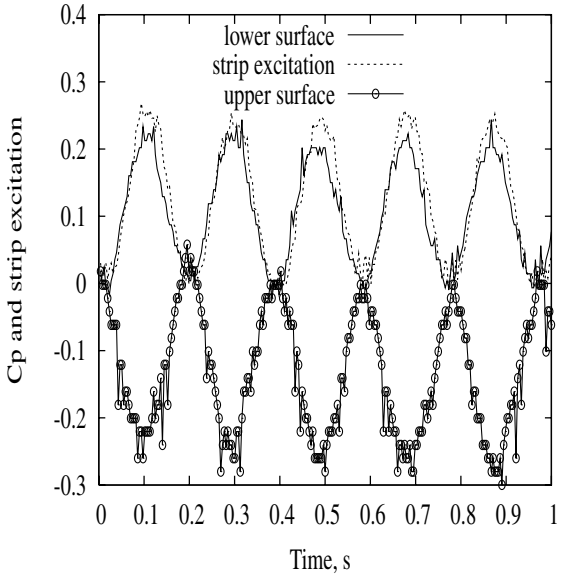

Fig. 13 Pressure coefficient vs time at $x/c = 0.054$ for $\alpha = 5$ deg, $\omega = 5.1$ Hz ($k = 0.204$), and $h_s = 2.5\%$c.

pitching-moment coefficients are calculated by ensemble-averaging a total of 20 recorded cycles and then integration of these pressures over the airfoil.

It was observed during the course of the test that a turbulent fluctuating pressure was found at angles of attack beyond stall onset both for steady and unsteady state responses. It is believed to be associated with flow separation and possibly a vortex passage over the leading-edge region. In this case, we used the SD380 signal analyzer to acquire the aerodynamic-pressure transfer function (output pressure and input small-strip displacement) for each chordwise position on the model surface. This analyzer has an ac-coupled function and a higher data acquisition specification than that of the NB-MIO-16 package. It provides a direct measurement of the transfer function, which is defined as the ratio of the *averaged* cross spectrum of the input–output to the *averaged* input power spectrum.

Results and Discussion

Static Results

A photograph of the experimental airfoil model in the wind tunnel is shown in Fig. 4.

For the theoretical calculations, an incompressible Navier–Stokes code INS2D, developed at NASA Ames Research Center, is employed. In the INS2D code, the discretized equations are solved using a third-order upwind finite difference method and the solution is implicitly advanced using a Gauss–Seidel-type line relaxation.

The computational grids were generated using the Gridgen code. The grid points are clustered along the surface of the airfoil and the leading and trailing edges to better resolve the flow features in these regions. The C-O grid has dimensions of 438×100. The far-field boundaries are eight chord lengths from the airfoil.

The boundary conditions are specified as follows. The airfoil surface is a static, no-slip, wall boundary condition. The pressure is obtained by specifying a zero wall-normal pressure gradient. The far-field outer boundary is computed using a characteristic relation for the pressure. At the downstream outflow boundary, a constant static pressure is used and the velocities are extrapolated from the interior. Along the wake-cut line of the C-grid, the pressure and velocities are obtained from an average of the surrounding values.

The Gurney flap is modeled by blanking out the grid points "inside" the flap. The surface of the flap is treated as a static no-slip wall.

The aerodynamic forces and moment on the airfoil are also obtained from the measured pressure distribution over the airfoil surfaces. The shear stress distribution is not measured in this work. Because of the smaller skin friction coefficient for the present model compared with the pressure coefficient, the error from neglecting the former is relatively small. Thus, we can approximately obtain the integral forms for the force and moment coefficients as follows:

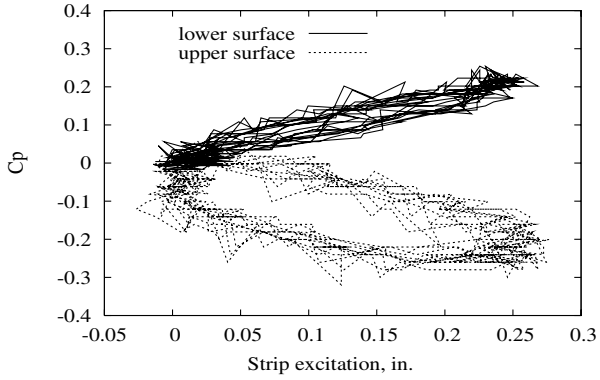

a) x/c=0.054

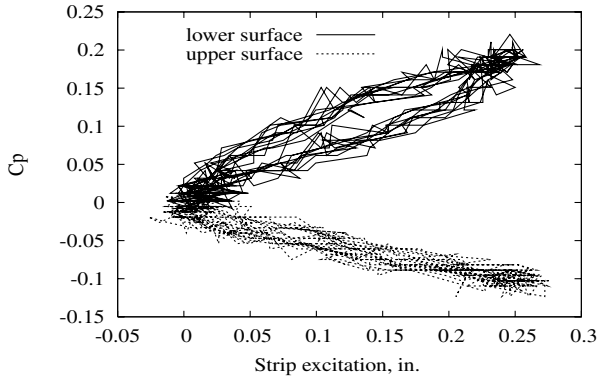

b) x/c=0.18

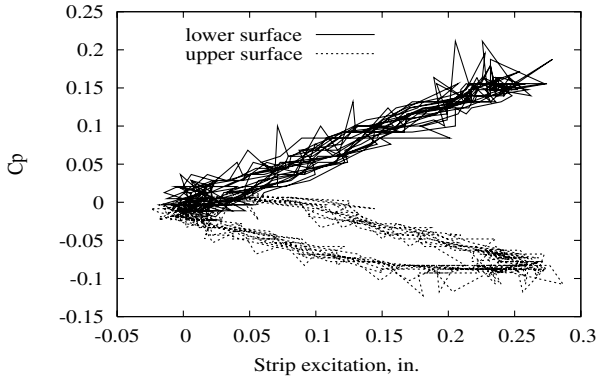

c) x/c=0.62

Fig. 14 Pressure hysteresis loop plots for $\alpha = 5$ deg, $\omega = 5.1$ Hz, $h_s = 2.5\%c$, and $U = 20$ m/s (65.6 ft/s).

$$C_l = \frac{\cos\alpha}{c}\int_0^c (C_{p,l} - C_{p,u})\,\mathrm{d}x - \frac{\sin\alpha}{c}\int_0^c \left(C_{p,u}\frac{\mathrm{d}y_u}{\mathrm{d}x} - C_{p,l}\frac{\mathrm{d}y_l}{\mathrm{d}x}\right)\mathrm{d}x \tag{1}$$

$$C_{m,c/4} = \frac{1}{c^2}\left[\int_0^c (C_{p,u} - C_{p,l})(x - c/4)\,\mathrm{d}x + \int_0^c \left(C_{p,u}\frac{\mathrm{d}y_u}{\mathrm{d}x}y_u\,\mathrm{d}x - C_{p,l}\frac{\mathrm{d}y_l}{\mathrm{d}x}y_l\right)\mathrm{d}x\right. \tag{2}$$

where $C_{p,l}$ and $C_{p,u}$ are the pressure coefficients on the lower and upper surfaces, respectively; y_l and $\mathrm{d}y_l/\mathrm{d}x$ and y_u and $\mathrm{d}y_u/\mathrm{d}x$ are the coordinates and slopes on the lower and upper surfaces, and $C_{m,c/4}$ is the pitching-moment coefficient about the quarter-chord.

The measured $C_{p,l}$ or $C_{p,u}$ only have 10 data over the chord. For convenient application of the integral over the chord, a polynomial

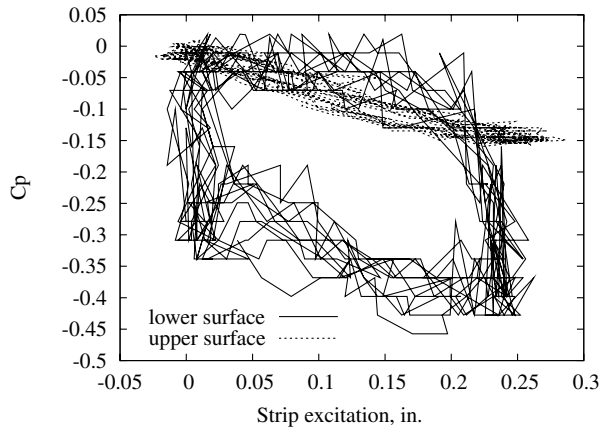

a) C_p vs h

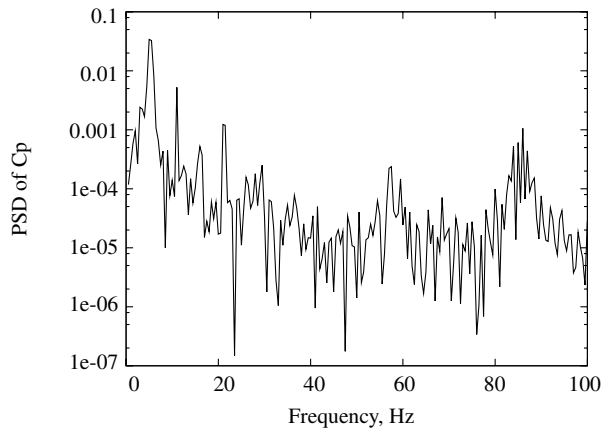

b) PSD plot

Fig. 15 Dynamic-pressure behavior at $x/c = 0.92$ for $\alpha = 5$ deg, $\omega = 5.1$ Hz, $h_s = 2.5\%c$, and $U = 20$ m/s (65.6 ft/s).

formula for the pressure coefficient ($C_{p,l}$ or $C_{p,u}$) vs the chordwise position x/c is constructed:

$$C_p(x/c) = \sum_{i=0}^{4} a_i (x/c)^i \tag{3}$$

where the a_i are determined by a least-squares curve-fitting method from the experimental data for C_p.

The lift and pitching-moment coefficients for the baseline clean configuration were calculated. A comparison of the measured and calculated lift and pitching-moment coefficients on the airfoil for angles of attack from 0 to 20 deg is shown in Figs. 5a and 5b, respectively. The theoretical and experimental lift and pitching coefficients for the small-strip height of 2.5%c are also presented in Figs. 5a and 5b for angles of attack from 0 to 20 deg. It is seen that the addition of the small strip produces a significant lift and pitching-moment coefficient increment compared with the baseline configuration. The results show that good correlation is observed between computation and experiment, except near the maximum lift and pitching-moment coefficients both for the clean configuration and with a small strip.

For smaller incidence (less than the static stall angle), $\alpha = 5$ deg, a typical theoretical and experimental pressure distribution along the upper and lower surfaces is shown in Fig. 6a for the case without the small strip, $h = 0$, and Fig. 6b for the case with the small strip, $h = 2.5\%$, respectively. Comparing Figs. 6a and 6b, the results show a significant pressure increase due to the small strip in the leading-edge suction peak, both for the theory and test. This is because of an increased circulation at the trailing edge due to the small strip. The results also show a significant pressure change for the chordwise

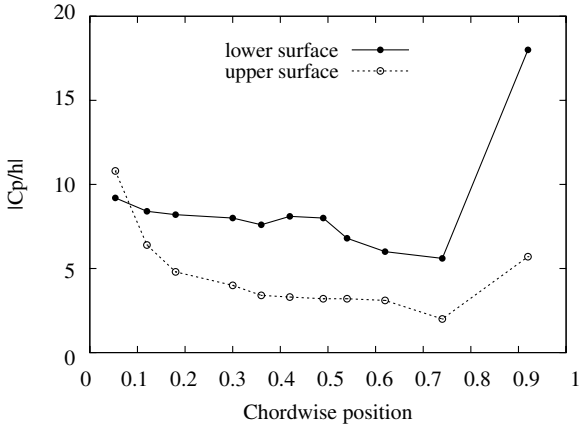

a) $|C_p/h|$

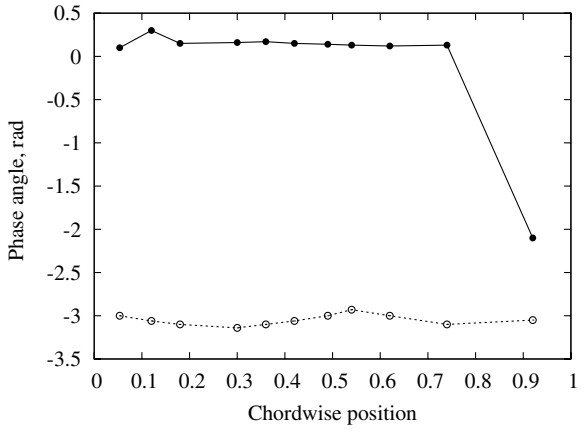

b) Ψ^{cp}

Fig. 16 Dynamic-pressure transfer function along the chordwise position for $\alpha = 5\,\text{deg}$, $\omega = 5.1$ Hz, $h_s = 2.5\%c$, and $U = 20$ m/s (65.6 ft/s).

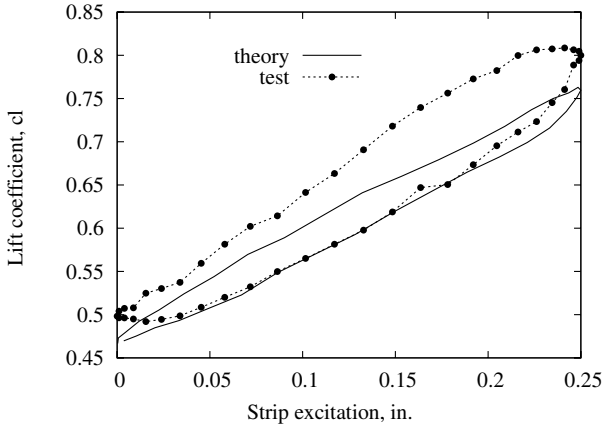

a) C_l vs h

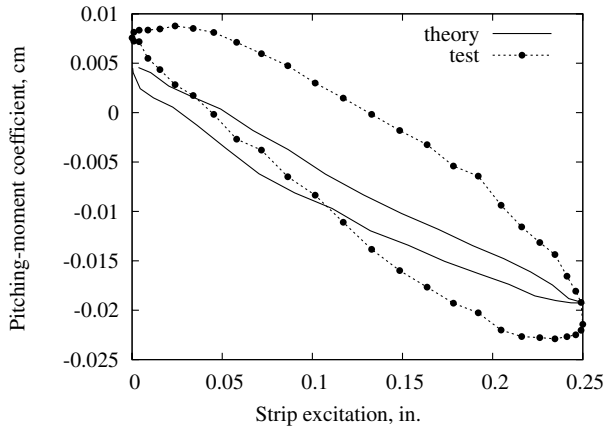

b) C_m vs h

Fig. 17 Theoretical and experimental aerodynamic hysteresis loop for $\alpha = 5\,\text{deg}$, $\omega = 5.1$ Hz, $h_s = 2.5\%c$ and $U = 20$ m/s (65.6 ft/s).

positions beyond the small-strip position (i.e., $x/c > 0.9$). There is a pressure jump (drop) near $x/c = 0.9$ for the lower surface on which the small strip exists. The experimental data at pressure tap $x/c = 0.92$ also show this pressure-jump phenomenon, as shown in Fig. 6b. This is because there is a flow reversal region in which a flow-separation phenomenon occurs. Figure 7a shows the time history of the lower- and upper-surface pressure coefficients vs time for $\alpha = 5\,\text{deg}$ at chordwise position $x/c = 0.92$. There are some irregular fluctuating pressures at both the lower and upper surfaces. But the fluctuating pressure at the lower surface is larger than that at the upper surface. It is believed the fluctuating pressure at the upper surface is created by a combination wind-tunnel freestream turbulence and by both boundary-layer flow separation and freestream turbulence for the lower surface. Wake-induced fluctuations may have also played a role. The results in Fig. 7b for $\alpha = 15\,\text{deg}$ will be discussed subsequently.

To better understand this phenomenon, a theoretical contour plot for the flow velocity in the x direction is shown in Fig. 8 for an incidence of $\alpha = 5$ deg. As shown in this figure, for the lower-surface region, there are two counter-rotating vortices of different sizes (in the figure, arrow A indicates an anticlockwise vortex of a smaller size and arrow B indicates a clockwise vortex of a larger size) directly downstream of the small strip on which the streamlines bounding the vortex region meet. This pattern is similar to that first hypothesized by Liebeck [1] and the measured data of Jeffrey et al. [2]. As shown for the upper-surface region, the streamline is smooth and there is no flow separation. From this figure, it is not difficult to understand the reason for the pressure phenomenon in the lower-surface region when $x/c > 0.9$.

For a larger incidence, $\alpha = 15$ deg (larger than the static stall angle of attack), the theoretical and experimental pressure distributions along the upper and lower surfaces are shown in Fig. 9. The pressure increase in the leading-edge suction peak is not as significant as for $\alpha = 5$ deg due to the stall flow and reduced circulation. The pressure change is significant near the trailing region. The effect of the small strip is to increase the pressure on the surface of the airfoil compared with the clean airfoil case. Similar to Fig. 6b, a pressure jump is found close to $x/c = 0.9$. The experimental measurement data are close to the theory and also show this pressure-jump phenomenon.

Figure 7b shows the time history of the lower- and upper-surface pressure coefficients vs time for $\alpha = 15$ deg at chordwise position $x/c = 0.92$. There are larger irregular fluctuating pressures at both the lower and upper surfaces. It is believed that the larger fluctuating pressures are created by the significant flow separation and the effect of wind-tunnel turbulence is smaller. The effect of the stall flow separation on the pressure coefficient is significant. Figure 10 shows the power spectral density (PSD) plot of the time histories of Fig. 7 for $\alpha = 5$ and 15 deg. The energy of the power spectrum concentrates in the lower-frequency region for $\alpha = 15$ deg and there is no evident peak amplitude in the power spectrum. For $\alpha = 5$ deg, the power spectrum is relatively flat.

A theoretical u velocity contour is shown in Fig. 11 for an incidence of $\alpha = 15$ deg. It can be also used to explain the jump phenomenon in Fig. 9b. Note that for a larger incidence, there is no longer a smooth streamline in the region of the upper surface. A larger flow separation in the trailing-edge region occurred because of the Gurney flap in addition to the usual boundary-layer separation that occurs over the upper surface when there is no Gurney flap.

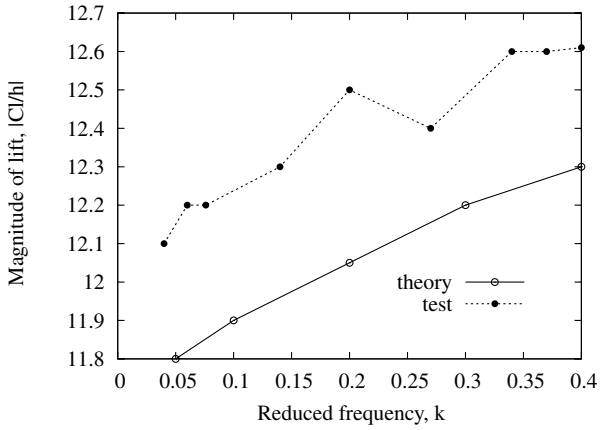

a) $|C_l/h|$

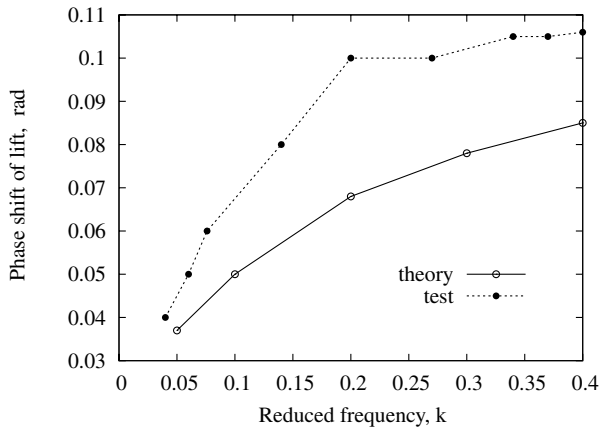

b) Ψ^{cl}

Fig. 18 Measured and computed aerodynamic-lift transfer function vs the reduced frequency for $\alpha = 5\,\text{deg}$, $h_s = 2.5\%c$, and $U = 20$ m/s (65.6 ft/s).

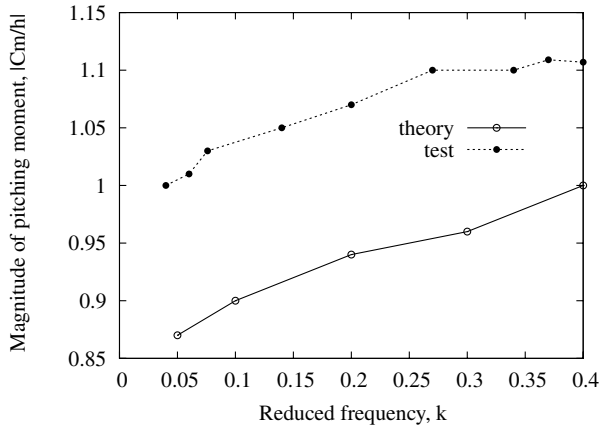

a) $|C_m/h|$

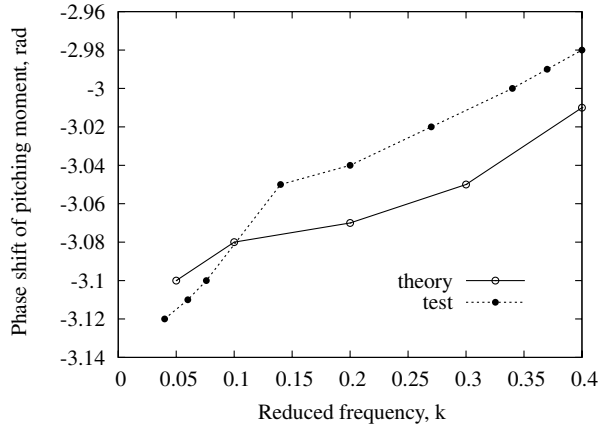

b) Ψ^{cm}

Fig. 19 Measured and computed pitching-moment transfer function vs the reduced frequency for $\alpha = 5\,\text{deg}$, $h_s = 2.5\%c$, and $U = 20$ m/s (65.6 ft/s).

For the present theoretical and experimental results for the steady-state aerodynamics of a two-dimensional airfoil, there are three points to be noted:

1) When the angle of attack is zero, there is a nonzero lift and the lift coefficient increases as the small-strip height increases. This is because there is an additional circulation due to a von Kármán vortex street of alternately shed vortices created by the small strip near the trailing edge.

2) The addition of a small strip increases the maximum lift coefficient from 0.92 up to 1.32 for the theory and from 0.9 up to 1.4 for the experiment for a small-strip height of $2.5\%c$. As shown in Fig. 7, the additional increase in circulation in the trailing-edge region increases the total lift coefficient of the airfoil.

3) With the addition of a small strip, there is a significant pitching-moment increase, as shown in Fig. 5b. A larger small-strip height leads to a larger pitch-down-moment coefficient.

Dynamic Results

The unsteady aerodynamic response data were acquired from an oscillating small-strip wing model. The oscillatory frequency varied from 1 to 10 Hz (i.e., the reduced frequency varied from $k = \omega b/U = 0.04$ to 0.4, with the maximum oscillating amplitude of the strip of $h_s = 6.35$ mm (0.25 in.) or $h_s = 2.5\%c$. The measured unsteady response data were for two typical steady angles of attack: an unstalled angle of attack, $\alpha = 5$ deg, and a stalled angle of attack, $\alpha = 15$ deg. These data were used to construct the linear aerodynamic transfer function and nonlinear (stall) statistical aerodynamic loadings for the case of an oscillating strip.

The nondimensional small-strip oscillation normalized by the chord is given by

$$h(t) = \frac{h_s}{2c}\left[1 + \sin\left(\frac{3\pi}{2} + \omega t\right)\right] \tag{4}$$

The nondimensional amplitude of the strip oscillation is $h_s/2c = 0.0125$. Note that the mean value of $h(t)$ is $h_s/2c$, the maximum value is h_s/c, and the minimum value is zero (see Fig. 12).

The measured aerodynamic transfer function $H_j^{\text{cp}}(\omega)$ for the pressure coefficient to the strip oscillating at the j chordwise position (both for the lower or upper pressure coefficient) is a nondimensional quantity and expressed as

$$H_j^{\text{cp}}(\omega) = Re_j^{\text{cp}}(\omega) + iIm_j^{\text{cp}}(\omega) \tag{5}$$

Because of the simple harmonic motion of both input and output signals, the measured aerodynamic transfer function is ideally determined from the ratio C_p/h of the output to input amplitude and the phase shift Ψ between output and input signals; that is,

$$\left|\frac{C_p}{h}\right|_j = \sqrt{(Re_j^{\text{cp}})^2(\omega) + (Im_j^{\text{cp}})^2(\omega)} \tag{6}$$

and

$$\Psi_j^{\text{cp}} = \tan^{-1}\frac{Im_j^{\text{cp}}(\omega)}{Re_j^{\text{cp}}(\omega)} \tag{7}$$

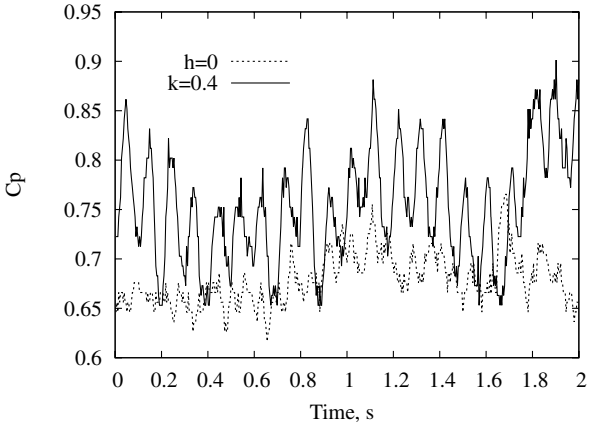

a) $C_{p,l}$ vs t

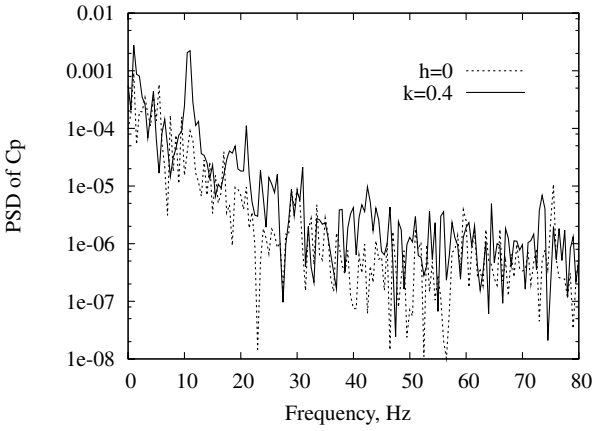

b) PSD of $C_{p,l}$

Fig. 20 Measured time history and PSD analysis on the lower surface for $\omega = 10$ Hz or $k = 0.4$; $\alpha = 15$ deg at $x/c = 0.92$ and $h_s/2c = 0.0125$.

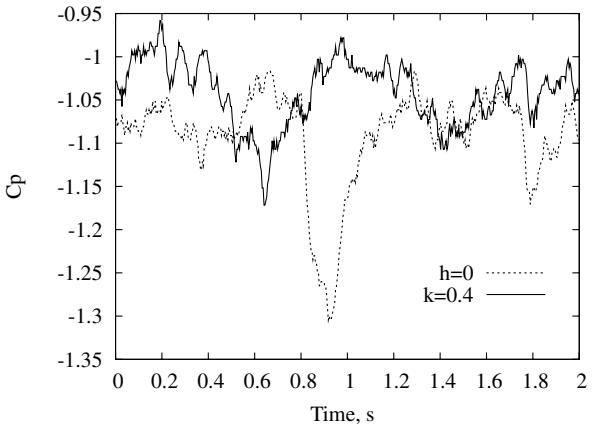

a) $C_{p,u}$ vs t

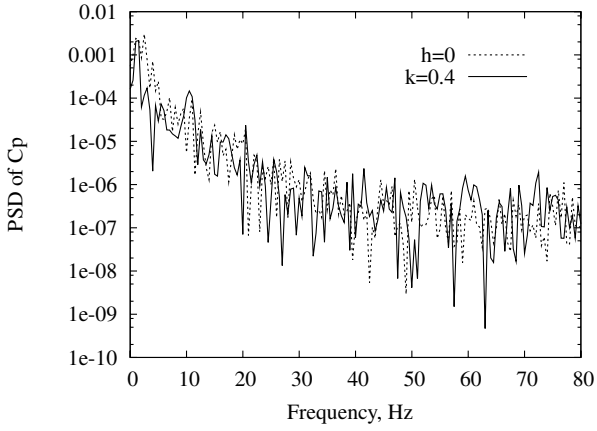

b) PSD of $C_{p,u}$

Fig. 21 Measured time history and PSD analysis on the upper surface for $\omega = 10$ Hz or $k = 0.4$; $\alpha = 15$ deg at $x/c = 0.92$ and $h_s/2c = 0.0125$.

However, the measured real and imaginary parts of the pressure, Re_j^{cp} and Im_j^{cp}, include the fluctuating pressure due to noise. The measured data show that the input can be regarded as a pure sinusoidal signal and the noise is only involved in the output pressure signal. Thus, the preceding method needs to be modified, as described next, to reduce the effect of noise on the signal.

Let the aerodynamic noise be a stationary random process with a zero average value, defined as $\eta(t)$. The output pressure difference on the airfoil surface can be represented as

$$C_p(t) = C_{p0}(t) + \eta(t)$$

The aerodynamic transfer function H_j^{cp} is defined as the ratio of the cross PSD of output–input to the auto PSD of the input.

$$H_j^{\mathrm{cp}} = \frac{S_{\mathrm{cp},h}(\omega)}{S_{h,h}(\omega)} = \frac{\tilde{S}_{\mathrm{cp},h}(\omega) + \Delta S_{\mathrm{cp},h,\eta}(\omega)}{\tilde{S}_{h,h}(\omega)} \tag{8}$$

where $S_{h,h}$ and $S_{\mathrm{cp},h}$ are the measured auto PSD of the input–output and the cross PSD, $\tilde{S}_{h,h}$ and $\tilde{S}_{\mathrm{cp},h}$ are the corresponding true values of PSD, and S_η and $\Delta S_{\mathrm{cp},h,\eta}$ are the noise auto and cross PSD.

If the aerodynamic noise is independent of the input and output signals, the the term $\Delta S_{\mathrm{cp},h,\eta}$ of the noise cross PSD should be zero. If the aerodynamic noise is dependent of the input and output signals, then increasing the ensemble-averaging number will effectively reject the noise.

Substituting Eq. (5) into Eqs. (1) and (2), one obtains the measured aerodynamic lift and pitching-moment transfer functions, expressed as

$$H^{\mathrm{cl}}(\omega) = Re^{\mathrm{cl}}(\omega) + iIm^{\mathrm{cl}}(\omega) \tag{9}$$

$$H^{\mathrm{cm}}(\omega) = Re^{\mathrm{cm}}(\omega) + iIm^{\mathrm{cm}}(\omega) \tag{10}$$

Aerodynamic Response for Unstalled Angle of Attack

A typical example of the unsteady pressure time history (taking 1 s from the total number of data points, 5120, or 10 s of total time history) obtained in this test is shown in Fig. 13 for incidence angle $\alpha = 5$ deg, $\omega = 5.1$ Hz, and $k = 0.204$ at the chordwise position $x/c = 0.054$. The output-pressure signal includes both the lower and upper pressure coefficients. For comparison, the input strip excitation motion is also plotted in this figure. The pressure response is almost sinusoidal, although there are also some random fluctuating pressures. From the time history, we also can construct a pressure hysteresis loop due to the strip-excitation motion, as shown in Fig. 14a for $x/c = 0.054$. For the pressure coefficient $C_{p,l}$ on the lower surface, a very small pressure hysteresis loop is found, and for the upper surface, there is a little larger hysteresis loop. For comparison, the pressure hysteresis loop plots at other chordwise positions (i.e., $x/c = 0.18$ and 0.62) are also plotted in this figure, as shown in Figs. 14b and 14c. In these chordwise positions, $C_{p,l}$ at the lower surface oscillates with the same phase angle as the strip oscillation, but the $C_{p,u}$ at the upper surface oscillates in opposed phase shift with respect to the strip oscillation.

Figure 15a shows the pressure hysteresis loop behavior, and Fig. 15b shows a PSD analysis of the lower-surface pressure at the chordwise position $x/c = 0.92$. For the lower-surface pressure, there is a larger phase shift between the input h and output $C_{p,l}$ (the phase angle changes from positive to negative), and the response motion of

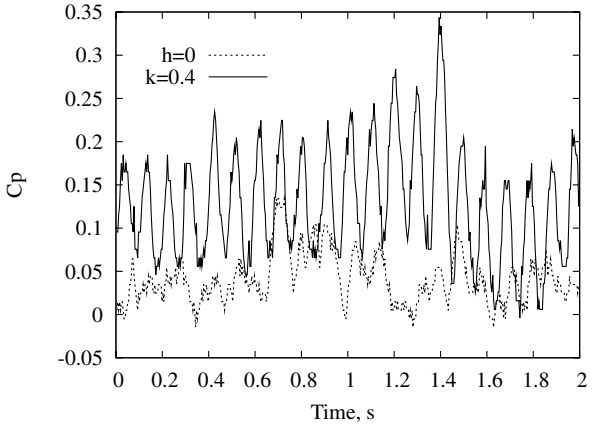

a) $C_{p,l}$ vs t

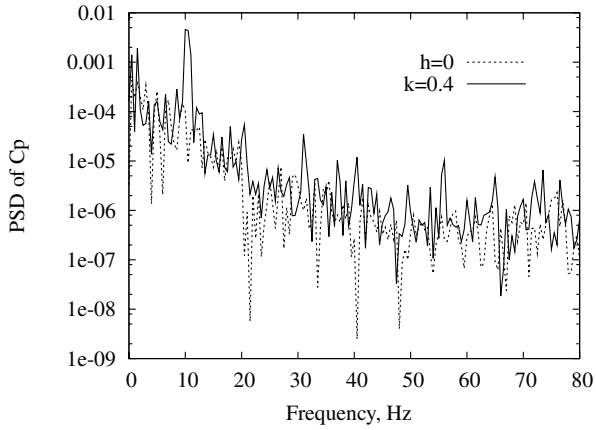

b) PSD of $C_{p,l}$

Fig. 22 Measured time history and PSD analysis on the lower surface for $\omega = 10$ Hz or $k = 0.4$; $\alpha = 15$ deg at $x/c = 0.92$ and $h_s/2c = 0.0125$.

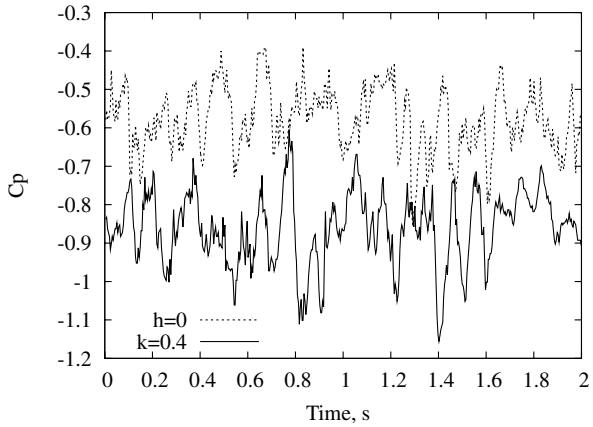

a) $C_{p,u}$ vs t

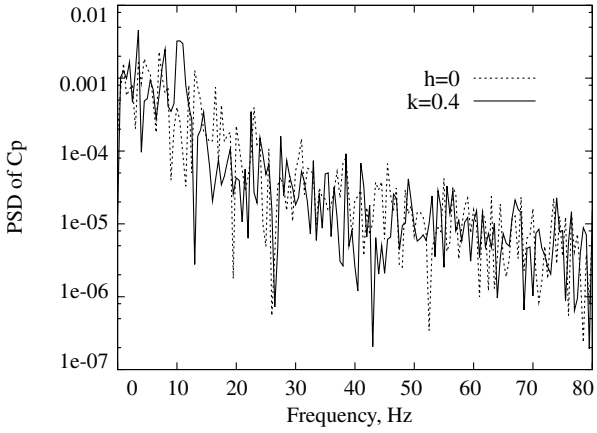

b) PSD of $C_{p,u}$

Fig. 23 Measured time history and PSD analysis on the upper surface for $\omega = 10$ Hz or $k = 0.4$; $\alpha = 15$ deg at $x/c = 0.92$ and $h_s/2c = 0.0125$.

$C_{p,l}$ becomes complex. As shown in Fig. 15b, there are many higher harmonic components in addition to the main frequency, $\omega = 5.1$ Hz. This is because there is a flow separation in this region.

When the pressure output signals are treated by a data-smoothing process [i.e., using Eq. (8)], the aerodynamic transfer function H_j^{cp} can be determined and plotted vs the chordwise position, as shown in Figs. 16a and 16b for $\alpha = 5$ deg, $\omega = 5.1$ Hz, and $U = 65.6$ ft/s. Figure 16a is for the magnitude $|C_p/h|$ of the aerodynamic transfer function and Fig. 16b is for the phase angle. Note that in this case, the input strip motion h is the amplitude of the strip oscillation and it is normalized by the chord. Thus, the magnitude $|C_p/h|$ is a nondimensional quantity. There is a pressure-jump phenomenon near $x/c = 0.9$ for the lower surface on which the small strip exists. In the region of $x/c = 0.9$, a flow-separation phenomenon occurs. This leads to a pressure jump for both the steady and unsteady flow aerodynamics.

The integrations of the chordwise pressure distribution were performed after verifying the cycle-to-cycle repeatability of the individual pressure transducer responses. A cycle-averaging procedure was used to smooth the pressure signals to obtain a good representation of the cyclical lift and moment responses. Typical results for $\omega = 5.1$ Hz or reduced frequency $k = 0.204$ are shown in Fig. 17a for the lift response hysteresis loop and 17b for the pitching-moment response. For comparison, the theoretical results predicted from the INS2D code are also plotted in this figure. For details of these calculations see Tang et al. [7]. Note that the time history calculated needs several cycles to achieve a steady state. The experimental and theoretical data both have a small phase shift. The experimental phase angle is about 0.11 rad for the lift coefficient and $-\pi + 0.1 = -3.04$ rad for the pitching-moment coefficient, and the theoretical phase angle is 0.065 deg and $-\pi + 0.07 = -3.07$ rad for the lift and pitching-moment coefficients. The reasons and consequences for this hysteresis are believed to be as follows.

1) There is an aerodynamic damping when the small strip oscillates. This damping varies with the reduced frequency of the oscillating strip.

2) Because of the oscillating strip, there is a flow-separation region near the chordwise position $x/c = 0.9$ and a pressure jump, as shown in Fig. 15a. This significantly affects the pitching-moment coefficient.

As shown in Fig. 17, the averaged lift and pitching-moment values over one oscillation cycle are $C_{l,\text{ave}} = 0.65$ and $C_{m,\text{ave}} = -0.007$ for the test, which are little larger than the static values $C_{l,\text{static}} = 0.47$ and $C_{m,\text{static}} = 0.0055$ for the case without a small strip. The oscillating amplitude for the lift and pitching moment are $C_{l,\text{dynamic}} = 0.155$ and $C_{m,\text{dynamic}} = -0.014$ for the test and 0.15 and -0.0125 for the theory. The agreement between the theory and experiment is reasonably good.

Using Eqs. (9) and (10), one obtains the measured and theoretical dynamic lift and pitching-moment transfer functions, the magnitudes $|C_l/h|$ and $|C_m/h|$, and the phase-shift angles Ψ^{cl} and Ψ^{cm}. In the present test, reduced frequencies of $k = 0.04$, 0.06,0.076,0.14,0.2, 0.34,0.37, and 0.4 are considered. The results are shown in Fig. 18 for the lift and Fig. 19 for the pitching moment. Figure 18a shows the magnitude of the transfer function and Fig. 18b shows the phase-shift angle. For comparison, the numerical data predicted from the INS2D code are also plotted in this figure. Calculated reduced frequencies of $k = 0.05$, 0.1, 0.2, 0.3, and 0.4 are used. Both the magnitude and phase-shift angle increase as the reduced frequency increases. The measured maximum magnitude increment is about 4.2% for the lift and 11% for the pitching-moment coefficients when the reduced frequency increases from $k = 0.04$ to 0.4. Note that the y scale was

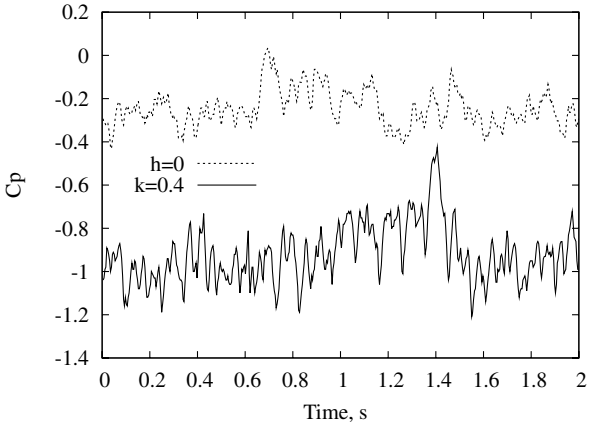

a) $C_{p,l}$ vs t

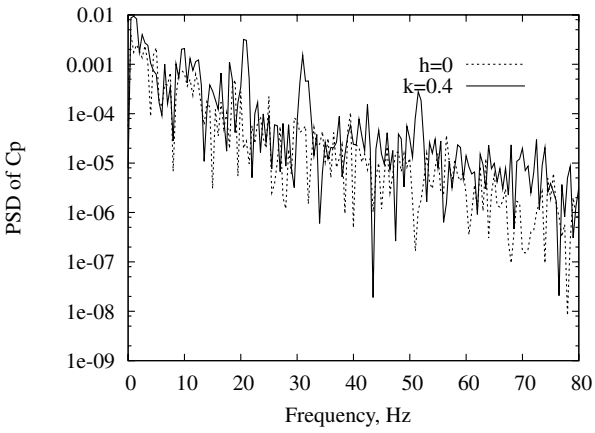

b) PSD of $C_{p,l}$

Fig. 24 Measured time history and PSD analysis on the lower surface for $\omega = 10$ Hz or $k = 0.4$; $\alpha = 15$ deg at $x/c = 0.92$ and $h_s/2c = 0.0125$.

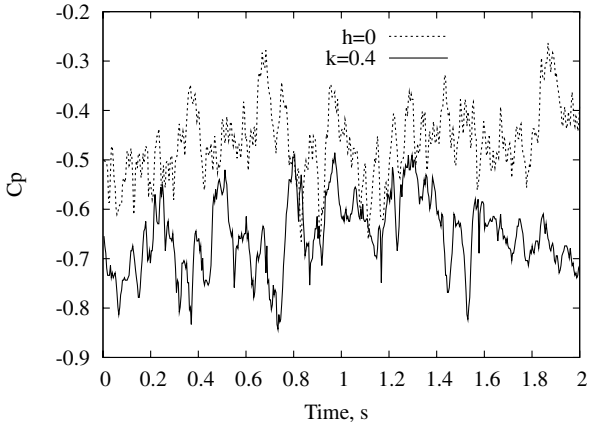

a) $C_{p,u}$ vs t

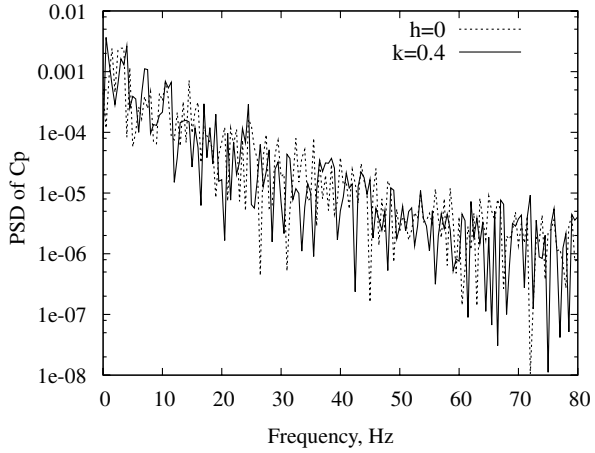

b) PSD of $C_{p,u}$

Fig. 25 Measured time history and PSD analysis on the upper surface for $\omega = 10$ Hz or $k = 0.4$; $\alpha = 15$ deg at $x/c = 0.92$ and $h_s/2c = 0.0125$.

exaggerated for clarity in these figures. The agreement between the numerical data and experimental results is reasonably good.

Aerodynamic Response for Stalled Angle of Attack

In this section, the flow regime is studied at $\alpha = 15$ deg. When the incidence increases from an unstalled to a stalled angle of attack, flow separation occurs and the separated region enlarges. The pressure signals on the airfoil surfaces in the flow-separation region are no longer periodic oscillations, even though the strip has a harmonic oscillation. Some typical examples of the unsteady-pressure time histories obtained in this test are shown in Figs. 20–25 for a strip-oscillation frequency of $\omega = 10$ Hz and $k = 0.4$ at three typical chordwise positions: $x/c = 0.12$, 0.49, and 0.92. Figures 20a, 21a, 22a, 23a, 24a, and 25a show the time histories for lower- and upper-surface pressure coefficients, respectively. Figures 20b, 21b, 22b, 23b, 24b, and 25b show the corresponding PSD analyses. For comparison, the results for the baseline clean configuration (no small strip, $h = 0$) are also shown in these figures.

Figures 20 and 21 show the dynamic-pressure behavior for the chordwise position near the leading edge of the airfoil, $x/c = 0.12$. As shown in Figs. 20a and 21a, the response includes a static pressure and a fluctuating pressure (dynamic part). The dynamic part is not periodic on the upper surface (in this flow-separation region, the turbulent fluctuating pressure is not small) and is near-periodic on the lower surface, as shown in PSD plots in Figs. 20b and 21b. As shown in Fig. 20b, there is a dominant peak at frequency $\omega = 10$ Hz and a very evident peak at about 0.5 Hz. This is believed due to the flow fluctuating in response to the strip oscillation. For the clean airfoil configuration, the turbulent fluctuating pressure is weaker for the lower surface and stronger for the upper surface. There is no dominant peak in the PSD plot and the energy of the power spectrum concentrates in the lower-frequency region. Because of the flow separation, the upper-surface pressure is still dominated by the turbulent fluctuations. The main frequency component (at $\omega = 10$ Hz) is relatively weak. A small peak at the main frequency is found in Fig. 21b. The oscillating strip does not significantly change the pressure behavior on the upper surface.

For estimating the effect of the oscillating strip on the aerodynamic loading, a statistical averaging method is used. In the present work, the whole sampled time history is 10 s with 5120 sampled points. Two statistically physical quantities over the whole sampled time history are considered in this section. One is an averaged static pressure $\bar{C}_p$ and the other is the rms value for the dynamic pressure, $|C_p|_{\text{rms}}$. In this case, for the static part, $\bar{C}_{p,l} = 0.76$ and $\bar{C}_{p,u} = -1.05$. For the dynamic part, the lower-surface pressure rms value is $|C_{p,l}|_{\text{rms}} = 0.035$ and the upper-surface rms value is $|C_{p,u}|_{\text{rms}} = 0.044$ at $x/c = 0.12$. For the clean airfoil ($h = 0$), $\bar{C}_{p,l} = 0.69$, $\bar{C}_{p,u} = -1.075$, $|C_{p,l}|_{\text{rms}} = 0.012$, and $|C_{p,u}|_{\text{rms}} = 0.05$, as shown in Fig. 20. Thus, the averaged static-pressure increment on the pressure side (lower surface) is about 10%. The dynamic rms value on the upper surface is larger than these on the lower surface for the clean airfoil ($h = 0$) due to the flow separation on the upper surface, but for the oscillating strip, the dynamic rms increases on the lower surface and slightly decreases on the upper surface. This suggests that the oscillating strip has changed the flow-separation character.

For a chordwise position near the midchord, $x/c = 0.49$, the results are shown in Figs. 22 and 23. The response motions are similar to the case for $x/c = 0.12$, but the periodicity of the pressure oscillations is stronger. The averaged static pressure is $\bar{C}_{p,l} = 0.12$ and $\bar{C}_{p,u} = -0.86$. The lower-surface-pressure dynamic rms

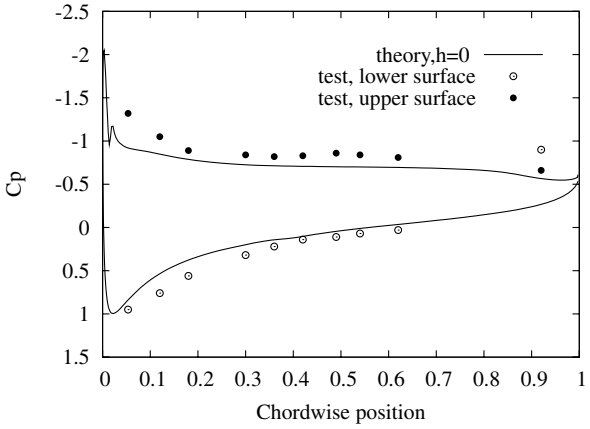

a) Averaged pressure

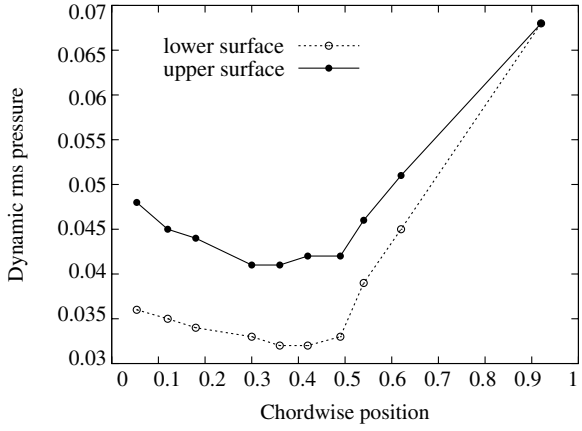

b) Dynamic rms pressure

Fig. 26 Measured averaged and dynamic rms pressures over the chord for $k = 0.4$, $\alpha = 15$ deg, $U = 20$ m/s (65.6 ft/s), and $h_s/2c = 0.0125$.

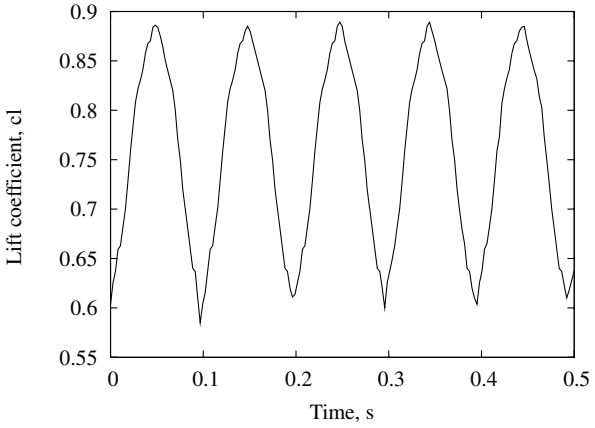

a)

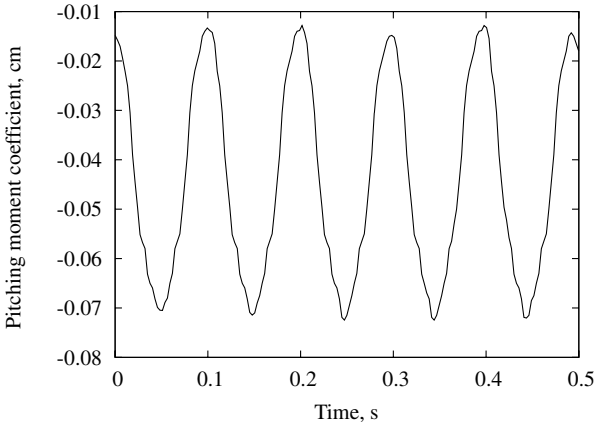

b)

Fig. 27 Time history of a) lift and b) pitching-moment coefficients for $\alpha = 15$ deg, $\omega = 10$ Hz ($k = 0.4$), $h_s = 2.5\%c$, and $Re = 348,000$.

value is $|C_{p,l}|_{\text{rms}} = 0.033$ and the upper-surface rms value is $|C_{p,u}|_{\text{rms}} = 0.086$. For the clean airfoil ($h = 0$), $\bar{C}_{p,l} = 0.01$, $\bar{C}_{p,u} = -.57$, $|C_{p,l}|_{\text{rms}} = 0.013$, and $|C_{p,u}|_{\text{rms}} = 0.078$. Both the static and oscillating pressures increase when the strip oscillates, especially on the pressure side. This is because the oscillating strip creates a strong additional circulation near the trailing edge that changes both the laminar and separated flow regions. The effect of the strip varies with chordwise position.

For the chordwise position near the trailing edge, $x/c = 0.92$, the results are shown in Figs. 24 and 25. Both the lower- and upper-surface pressures show a stronger turbulent fluctuating flow in addition to the main frequency component. There are several evident peaks at harmonics of the main frequency for the lower-surface pressure. This is different from the static strip excitation, as shown in Fig. 7a for the time history and Fig. 10 for the PSD plot in the case of $\alpha = 15$ deg. The averaged static pressure is $\bar{C}_{p,l} = -0.9$ and $C_{p,u} = -0.63$. The lower-surface-pressure dynamic rms value is $|C_{p,l}|_{\text{rms}} = 0.068$ and the upper-surface rms value is $|C_{p,u}|_{\text{rms}} = 0.063$. However, for the clean airfoil ($h = 0$), $\bar{C}_{p,l} = -0.25$, $\bar{C}_{p,u} = -.48$, $|C_{p,l}|_{\text{rms}} = 0.041$, and $|C_{p,u}|_{\text{rms}} = 0.072$. The dynamic rms values show a slight change when compared with those of the oscillating strip, but the averaged static pressure on the pressure side has a significant change. The results are very similar to those from the discussion of the pressure-jump phenomenon in the section titled Aerodynamic Response for Unstalled Angle of Attack.

The measured static and dynamic-pressure distributions at other chordwise position were also obtained. The results are shown in Figs. 26a and 26b for a reduced frequency of $k = 0.4$. Figure 26a is the averaged static pressure and Fig. 26b is the dynamic rms values vs chordwise position. For comparison, the theoretical static pressure for the clean airfoil configuration is also plotted in Fig. 26a. Comparing Fig. 26a with Fig. 9b, an oscillating strip shows a greater increase of the aerodynamic loading than does the static strip.

Integrating the lower and upper pressure distribution over the chordwise position, one obtains averaged static lift and pitching-moment coefficients, as was discussed in the Static Results section. The averaged lift coefficient $\bar{C}_l$ is 0.83 and the pitching-moment coefficient $\bar{C}_m$ is -0.07. For comparison, the numerical results predicted from the INS2D code for $Re = 348,000$ and strip oscillation frequency of 10 Hz are shown in Figs. 27a and 27b. The theoretical averaged static lift and pitching-moment coefficients are 0.75 and -0.045, respectively. The agreement between the theory and experiment is reasonably good for the lift. There is a larger error for the averaged pitching-moment coefficient.

For other oscillating frequencies or other reduced frequencies k, the experimental results are shown in Fig. 28 for the averaged lift and pitching-moment coefficients vs the reduced frequency. The theoretical calculations consider five strip oscillating frequencies: that is, $\omega = 1.25$, 2.5, 5, 7.5, and 10 Hz ($k = 0.05$,0.1,0.2, 0.3, and 0.4). For the comparison, the measured averaged *static* results for $h = 1.25\%$ (mean height of the GF) are also plotted in these figures. From these figures, the following key points are noted:

1) The averaged aerodynamic loadings (lift and pitching moment) increase as the reduced frequency increases. The increment is evident for the pitching moment from -0.047 at $k = 0.04$ to -0.07 at $k = 0.4$, but for the lift, the increment is smaller: from 0.78 at $k = 0.04$ to 0.83 at $k = 0.4$. This is because the pitching moment is more sensitive than the lift when the oscillating source (strip oscillation) is located near the trailing edge.

2) The averaged aerodynamic loading benefit obtained from the oscillated strip near the trailing edge is less than the static strip

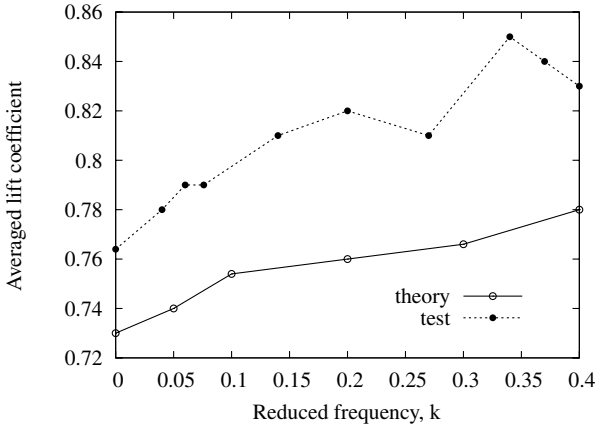

a)

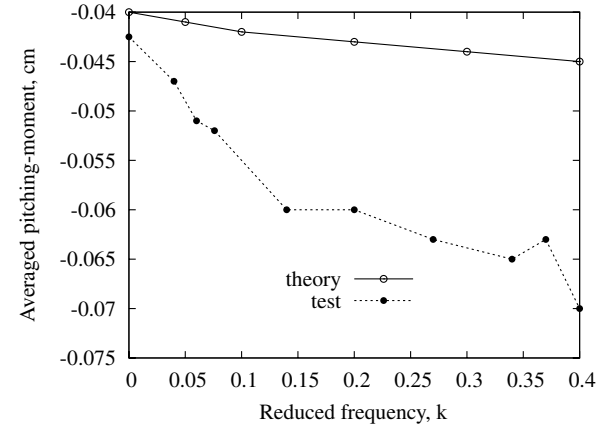

b)

Fig. 28 Time-averaged a) lift and b) pitching-moment coefficients vs the reduced frequency for $\alpha = 15\,\mathrm{deg}$, $h_s = 2.5\%c$, and $Re = 348,000$.

(Gurney flap) with the *same maximum height*. When the strip height is $h = 1.25\%$, the static lift coefficient is 0.91. However, when the strip height is $h = 1.25\%$ [i.e., the time-averaged or mean amplitude of the strip excitation (see Fig. 12)], the static lift coefficient ($k = 0$) is 0.764, whereas the maximum lift coefficient is 0.85 at $k = 0.34$. The corresponding static pitching-moment coefficient is -0.0425, whereas the maximum pitching-moment coefficient is -0.07 at $k = 0.4$. The results for the time-averaged or mean amplitude of strip excitation are shown at zero reduced frequency in Fig. 28.

3) The dynamic rms aerodynamic loading obtained from the oscillating strip is larger than that for the case of $h = 0$. The major contribution comes from the periodic pressure on the pressure side (lower surface). In the region of the flow separation (i.e., most of the upper surface), the contribution is smaller.

Conclusions

Steady and unsteady aerodynamic flow control using an oscillating small strip (Gurney flap) near the trailing edge on the lower surface was numerically and experimentally studied using Navier–Stokes code INS2D and wind-tunnel tests. The following conclusions are drawn:

1) Both a static and an oscillating small strip (Gurney flap) provide lift and pitching-moment enhancements.

2) For an unstalled angle of attack, an aerodynamic transfer function relative to the oscillated strip input provides a good understanding of the effects of the strip oscillation on the aerodynamic loadings. The lift and pitching-moment magnitudes of the transfer function increase as the reduced frequency is increased, and the incremental value is about 5% for the lift and 10% for the pitching moment, compared with the mean height of an oscillated GF. The experimental results show a pressure phase shift between the input and output. An aerodynamic-loading hysteresis phenomenon was found. Note that the oscillating Gurney flap does *not* behave like a static flap with a mean position of the oscillating flap, except at very low reduced frequencies.

3) For a stall angle of attack of 15 deg, a statistical averaging method is used to describe the effects of the strip oscillation on the stall aerodynamic loadings. Statistically averaged lift and pitching-moment coefficients and a dynamic rms aerodynamic response to the oscillating strip provide a reasonable representation for the stall aerodynamic loadings. The strip oscillating frequency has a discernible effect. Both the lift and pitching-moment coefficients increase by increasing the reduced frequency. The incremental increase is about 9% for the lift and a substantially larger increment for the pitching moment, compared with the mean height of an oscillated GF.

4) The agreement between the theory and experiment is reasonably good. The experimental results confirm the idea that an oscillating small strip located near the trailing edge can be a possible dynamic device for active aerodynamic flow control of a wing. The major differences between theory and experiment are thought to be due to the limitations of the turbulence model in the theory.

5) Finally, a comment on shedding frequencies is offered. The reduced frequency for shedding can arise from two sources. One is the shedding from the airfoil itself when placed at high angle of attack and the other is shedding from the Gurney flap per se. Both can be characterized in terms of a reduced frequency based upon an appropriate length scale. For the airfoil at high angle of attack, the relevant length scale is the airfoil chord multiplied by the sine of the angle of attack. For the Gurney flap, it is the height of Gurney flap. For the airfoil chord, stall angle of attack, and Gurney flap height relevant to our experiment, all of these frequencies may be converted to a common reduced frequency based upon the airfoil chord alone to compare them. The airfoil shedding reduced frequency based upon chord is about 1.2 and the Gurney flap shedding reduced frequency based upon airfoil chord is about 28, compared with the range of reduced frequencies studied in our paper of 0.0 to 0.4. Thus, the shedding frequencies are much higher than those studied for the oscillating Gurney flap in the present work.

Acknowledgments

This work was supported under the U.S. Air Force Office of Scientific Research grant, "Dynamics and Control of Nonlinear Fluid-Structure Interaction," under the direction of Dean Mook and Clark Allred. We would like to thank Peter Attar for his participation in the theoretical calculations.

References

[1] Liebeck, R. H., "Design of Subsonic Airfoil for High Lift," *Journal of Aircraft*, Vol. 15, No. 9, 1978, pp. 547–561.

[2] Jeffrey, D., Zhang, X., and Hurst, D. W., "Aerodynamics of Gurney Flaps on a Single-Element High-Lift Wing," *Journal of Aircraft*, Vol. 37, No. 2, 2000, pp. 295–301.

[3] Van Dam, C. P., Yen D. T. and Vijhen, P. M. H. W., "Gurney Flap Experiments on Airfoil and Wings," *Journal of Aircraft*, Vol. 36, No. 2, 1999, pp. 484–486.

[4] Storms, B. L., and Jang, C. S., "Lift Enhancement of an Airfoil Using a Gurney Flap and Vortex Generators," *Journal of Aircraft*, Vol. 31, No. 3, 1994, pp. 542–547.

[5] Greenblatt, D., and Wygnanski, I., "Dynamic Stall Control by Periodic Excitation, Part 1: NACA0015 Parametric Study," *Journal of Aircraft*, Vol. 38, No. 3, 2001, pp. 430–438.

[6] Greenblatt, D., Neuburger, D., and Wygnanski, I., "Dynamic Stall Control by Intermittent Periodic Excitation, "*Journal of Aircraft*, Vol. 38, No. 1, 2001, pp. 188–190.

[7] Tang, Deman, and Dowell, E. H., "Aerodynamic Flow Control of An Airfoil with Small Trailing Edge Strips," *Journal of Aircraft*, Vol. 43, No. 6, 2006, pp. 1854–1866.

[8] Gerontakos, P., and Lee, T., "Oscillating Wing Loadings with Small Trailing-Edge Strips," *Journal of Aircraft*, Vol. 43, No. 2, Mar.–Apr., 2006, pp. 428–436.

[9] Matalanis, C. G., and Eaton, J. K., "Wake Vortex Control Using Static Segmented Gurney Flaps," *AIAA Journal*, Vol. 45, No. 2, 2007, pp. 321–328.